THE JOURNAL OF PHYSICAL CHEMISTRY C

Subscriber access provided by UNIV OF CAMBRIDGE

Article

The Parameter Space of Graphene CVD on Polycrystalline Cu

Piran Ravichandran Kidambi, Caterina Ducati, Bruno Dlubak, Damian Gardiner, Robert S Weatherup, Marie-Blandine Martin, Pierre Seneor, Harry Coles, and Stephan Hofmann

J. Phys. Chem. C, **Just Accepted Manuscript** • Publication Date (Web): 27 Sep 2012

Downloaded from http://pubs.acs.org on September 28, 2012

Just Accepted

"Just Accepted" manuscripts have been peer-reviewed and accepted for publication. They are posted online prior to technical editing, formatting for publication and author proofing. The American Chemical Society provides "Just Accepted" as a free service to the research community to expedite the dissemination of scientific material as soon as possible after acceptance. "Just Accepted" manuscripts appear in full in PDF format accompanied by an HTML abstract. "Just Accepted" manuscripts have been fully peer reviewed, but should not be considered the official version of record. They are accessible to all readers and citable by the Digital Object Identifier (DOI®). "Just Accepted" is an optional service offered to authors. Therefore, the "Just Accepted" Web site may not include all articles that will be published in the journal. After a manuscript is technically edited and formatted, it will be removed from the "Just Accepted" Web site and published as an ASAP article. Note that technical editing may introduce minor changes to the manuscript text and/or graphics which could affect content, and all legal disclaimers and ethical guidelines that apply to the journal pertain. ACS cannot be held responsible for errors or consequences arising from the use of information contained in these "Just Accepted" manuscripts.

ACS Publications
High quality. High impact.

The Journal of Physical Chemistry C is published by the American Chemical Society. 1155 Sixteenth Street N.W., Washington, DC 20036

Published by American Chemical Society. Copyright © American Chemical Society. However, no copyright claim is made to original U.S. Government works, or works produced by employees of any Commonwealth realm Crown government in the course of their duties.

The Parameter Space of Graphene CVD on Polycrystalline Cu

Piran R. Kidambi[1], Caterina Ducati[2], Bruno Dlubak[1], Damian Gardiner[1], Robert S. Weatherup[1], Marie-Blandine Martin[3], Pierre Seneor[3], Harry Coles[1] and Stephan Hofmann[1,]

[1]Department of Engineering, University of Cambridge, Cambridge CB3 0FA, UK

[2]Department of Materials Science and Metallurgy, University of Cambridge, Cambridge CB2 3QZ, UK

[3]Unité Mixte de Physique CNRS/Thales, 91767 Palaiseau, France and Université de Paris-Sud 11, 91405 Orsay, France

Abstract

A systematic study on the parameter space of graphene CVD on polycrystalline Cu foils is presented, aiming at a more fundamental process rationale in particular regarding the choice of carbon precursor and mitigation of Cu sublimation. CH_4 as precursor requires H_2 dilution and temperatures ≥1000°C to keep the Cu surface reduced and yield a high quality, complete monolayer graphene coverage. The H_2 atmosphere etches as-grown graphene, hence maintaining a balanced CH_4/H_2 ratio is critical. Such balance is more easily achieved at low pressure conditions, at which however Cu sublimation reaches deleterious levels. In contrast, C_6H_6 as precursor requires no reactive diluent and consistently gives similar graphene quality at 100-150°C lower temperatures. The lower process temperature and more robust processing conditions allow the problem of Cu sublimation to be effectively addressed. Graphene formation is not inherently self-limited to a monolayer for any of the precursors. Rather, the higher the supplied carbon chemical potential the higher the likelihood of film inhomogeneity and primary and secondary multilayer graphene nucleation. For the latter, domain boundaries of the inherently polycrystalline CVD graphene offer pathways for a continued carbon supply to the catalyst. Graphene formation is significantly affected by the Cu crystallography, i.e. the evolution of microstructure and texture of the catalyst template form an integral part of the CVD process.

Keywords: mono and few-layer graphene (M/FLG), chemical vapor deposition (CVD), copper (Cu), polycrystalline, methane (CH_4), benzene (C_6H_6)

email: sh315@cam.ac.uk

Introduction

Economic, large-area growth combined with viable front and back-end integration strategies of mono and few-layer graphene (M-/FLG) are key requirements for the commercial exploitation of graphene's unique properties. Chemical vapor deposition (CVD) is the most promising route towards M-/FLG production and integration, based on its versatility and success with other nanomaterials.[1–3] While progress has been made in achieving MLG CVD over large areas,[4,5] the underlying growth mechanisms have yet to be fully understood[6–8] and the often narrow empirical process optimizations allow little generalization due to the vast CVD parameter space.[4,5,9–13] Most current literature focuses on exposing polycrystalline Cu[4,5] foils to methane (CH_4) at low pressures (LP) and high temperatures (≥1000°C). As-grown graphene can be fully continuous, but is inherently polycrystalline,[10] with MLG domain sizes typically ≤ 5μm in dimension.[10–12] Recent efforts have focused on increasing the MLG domain size,[12,13] but in general the compromise made to achieve high quality CVD graphene is to face undesirably high levels of Cu sublimation.[14]

Here, we focus on understanding graphene formation on polycrystalline Cu foils via a systematic exploration of the wider CVD parameter space, in particular regarding the choice of carbon precursor and mitigation of Cu sublimation, aiming at more rational process design. For CH_4 as precursor we find that, in agreement with previous literature, [4,5,9–12] uniform, high quality MLG growth is restricted to a rather narrow CVD parameter set of LP conditions, H_2 dilution and temperatures ≥1000°C, at which Cu sublimation is at deleterious levels. The H_2 atmosphere is required to keep the Cu surface reduced, but at the same time can etch as-grown graphene. Hence maintaining a balanced CH_4/H_2 ratio is critical, which makes the CH_4 based CVD process so delicate. In contrast, we find that benzene (C_6H_6) as precursor requires no reactive diluent, i.e. no delicate balance to be maintained, and consistently gives similar graphene quality at 100-150°C lower temperatures compared to CH_4 based CVD. The lower process temperature and more robust processing conditions allow the problem of Cu sublimation to be effectively addressed. Our growth study shows that Cu catalyzed CVD graphene formation is not inherently self-limited to a mono-layer. Rather we find the nucleation density, percentage of multi-layer nuclei and film uniformity/quality to critically depend on CVD conditions and growth kinetics. We suggest that the domain boundaries of the inherently polycrystalline CVD graphene offer pathways for the precursor to reach the catalyst even after complete MLG coverage. Our data further emphasizes that the Cu catalyst

template is not static and that the involved kinetics of grain growth are highly process dependent, making this an important process step for controlled graphene CVD.

Experimental Methods

Graphene synthesis is carried out in a customized cold-wall, low pressure CVD reactor (LPCVD, a heavily modified Aixtron BM3, base pressure ~ 5×10^{-6} mbar) and a hot-wall, atmospheric pressure furnace (APCVD). For LPCVD the total pressure (0.001 – 100 mbar) was regulated by a pressure controller at the reactor outlet. Commercial, cold-rolled Cu foils of different thicknesses and purities (Alfa Aesar Puratronic 99.999% purity, 25 μm and 100μm thick; Advent Research Materials, 99.995% purity, 12 μm thick) are used as catalysts. A one step CVD recipe is used as benchmark process for all systems. For all CVD recipes, heating up and pre-annealing is carried out in H_2 at 1000°C (LPCVD 4 mbar total pressure, heating rate ~250°C/min to 800°C followed by 50°C/min to 1000°C, APCVD heating rate ~ 40°C/min), after which the temperature is stabilized at the chosen growth temperature. In the case of CH_4 as the precursor, CH_4 is added to the annealing gas and cooling is performed in pure Ar (LPCVD cooling ramp ~150°C/min to 400°C at 7 mbar, APCVD cooling rate ~30°C/min). For C_6H_6 LPCVD, the exposure is to C_6H_6 (>99.7% purity, Sigma-Aldrich) without H_2 and cooling is performed in vacuum.

Samples were characterized by scanning electron microscopy (SEM, Philips XL30, 1-2 kV) and Raman spectroscopy (Renishaw InVia spectrometer, 532 nm excitation). For the latter the M-/FLG was typically transferred to SiO_2(300 nm)/Si substrates, using a polymethylmethacrylate (PMMA) support layer and a 0.5 M aqueous solution of $FeCl_3$ to etch the Cu foil. Acetone was then used to dissolve the PMMA support. Hall-bar devices were fabricated via e-beam lithography. Graphene layers, transferred to SiO_2/Si wafer substrates, were etched by an O_2 plasma and Au/Ti contacts evaporated on top. All electrical measurements were performed at room temperature. Electron backscattered diffraction (EBSD) experiments were performed in a FEI Helios Dual beam microscope (5-15 kV, current ~5.5 nA, working distance ~5-6.5 mm and sample tilt of ~ 60° with respect to the electron beam) with an Oxford Instruments - HKL EBSD Nordlys II detector in spot mode using Channel 5 software. Birefringence measurements followed the method outlined by Kim *et al.*[15] Liquid crystals of 4-pentyl-4`-cyanobiphenyl (5CB, Merck GmbH) were drop cast

onto graphene transferred to a glass substrate. A thin cover slip was added on top and measurements were carried out with the as-prepared sample placed between 2 crossed polarizers on a rotatable stage.

Results

The process of graphene formation on metal surfaces comprises nucleation, a subsequent expansion of the nuclei into domains, followed by a merging of the domains into a continuous covalently bonded film.[16] Here we refer to domains as regions that grow from a single nucleation point. Figure 1 shows SEM images of the Cu surface after short CH_4/H_2 exposures (see process details in caption), i.e. the early stages of CVD before the graphene coverage is continuous. Clear differences can be already seen for the different CVD conditions. Figs. 1 a,b and 1 c,d compare low (1:10) and high (1:1) CH_4/H_2 ratios for LPCVD conditions. For the former we observe MLG domains ranging from typically ~30-40μm^2 in size, with a few isolated areas (2-4μm^2) of FLG (as seen by SEM contrast and confirmed by Raman spectroscopy, see below). This is largely consistent with recent literature on optimized CVD with CH_4 on Cu foils.[4,5,9–13] We note that, due to the pressure regulation and backfilling procedure, the CH_4/H_2 ratio for our process is initially lower at the point of CH_4 addition, and thus partly resembles two step exposures reported in literature.[17] A higher CH_4 partial pressure (Fig. 1 c,d) leads to predominantly multilayer graphene nucleation and decreased sample homogeneity. This highlights that at the initial stages of growth, which we refer to the as primary nucleation stage, Cu is not inherently limiting graphene formation to a monolayer.

Figures 1 e-j highlight that the nature of graphene nucleation and growth at the early stages is highly dependent on catalyst surface orientation and impurity levels. Figs. 1 e,f show that for the same CVD conditions the resultant graphene coverage is different on adjacent Cu facets, with the imaged Cu (111) surface showing less graphene coverage compared to the Cu (110) surface. APCVD conditions as in Figs. 1 g,h and 1 i,j result in predominantly multilayer nucleation pattern. The nucleation density is notably increased and the shape of nuclei significantly changed for a Cu foil of lower purity (Figs. 1 i,j) at otherwise identical APCVD conditions. The FLG nuclei preferentially decorate Cu grain boundaries and appear aligned along the rolling striations of the foil. We find that a variation from 25-100 μm in foil

thickness does not appear to influence the kinetics of graphene formation on that scale (Figs. 1 c-f), but the foil thickness does influence the Cu grain growth kinetics as discussed in the following.

Figure 2 shows the results of EBSD analysis marked across SEM images of Cu foil surfaces for various process stages and conditions, highlighting the effects of Cu recrystallization and grain growth. Rolling striations are a dominant feature of the as-received Cu foils, for which EBSD shows Cu grain sizes < 2 μm with diverse surface orientations (Fig. 2 a, Table S1). We find the detailed deformation texture of the used commercial cold-rolled Cu foils to vary, despite being advertised as the same product. Hence the starting point cannot be automatically assumed as constant. It should be noted that here we do not use any additional Cu surface treatment procedure, such as electropolishing.[18] After annealing in H_2 at 1000°C, the Cu grain sizes increase to ~50 μm - 500 μm for APCVD and ~50 μm - 2 mm for LPCVD conditions (Figs. 2 b,c), which exceed the foil thickness. Whilst for APCVD we still find a crystallographically diverse Cu surface (Fig. 2b), the texture after LPCVD annealing becomes (111) dominated (Fig. 2c). The surface topography appears rougher and stepped for LPCVD conditions (Fig. 2c inset, with individual steps of ~10-50 nm) compared to the relatively smooth surface seen for APCVD conditions. The Cu grain size and orientation distributions are similar before and after hydrocarbon exposure (Figs. 2 d,e), most notably a (111) dominated texture for LPCVD conditions is maintained and several orientations are seen for APCVD.A polycrystalline material has no equilibrium structure, but depending on processing reaches a metastable equilibrium where the total grain boundary energy is locally minimized. At the given conditions, recrystallization followed by normal and abnormal grain growth are expected[19] and Fig. 2 is consistent with that. Our data emphasizes that the Cu catalyst template is not static and that the involved kinetics of grain growth are highly process dependent, making this an important process step for controlled graphene CVD.

We note that most literature directed towards the optimization of uniform MLG CVD focuses on low pressure conditions in the mbar range[9,17] during H_2 pre-treatment and CH_4/H_2 exposure, similar to our LPCVD conditions of Figs. 1 a,b and 2e. Based on their prevalence, we choose these LPCVD conditions as the standard "reference" for our further parametric study. Our discussion below will highlight why achieving continuous MLG films based on APCVD is very challenging using CH_4 as precursor. Figure 3 highlights the quality of graphene grown at our "reference" CH_4 based LPCVD conditions. Fig. 3a shows an optical

1
2
3
4
5
6
7
8
9
10
11
12
13
14
15
16
17
18
19
20
21
22
23
24
25
26
27
28
29
30
31
32
33
34
35
36
37
38
39
40
41
42
43
44
45
46
47
48
49
50
51
52
53
54
55
56
57
58
59
60

image of as-grown MLG transferred to a SiO_2 (300nm)/Si substrate. A corresponding Raman spectrum in Fig. 3b with G (~1600 cm^{-1}, FWHM ~ 23-25 cm^{-1}), D (~1360 cm^{-1}) and 2D (~2700 cm^{-1}, FWHM ~35-37 cm^{-1} which can be fitted with a single Lorentzian function) peaks as well as ratios of I_{2D}/I_G ~3.5 and I_D/I_G ~0.05 demonstrate the high quality of the MLG.[3,19] Figs. 3 c, e show Raman I_{2D}/I_G and I_D/I_G maps of the MLG (dimensions 50 μm × 50 μm), respectively, along with the corresponding distribution statistics (Figs. 3 d,f). The maps show average values of I_{2D}/I_G ~ 3.5 and I_D/I_G ~ 0.05 over a large area. 6 contact Hall geometry devices (Fig. 3g) give sheet resistances (on SiO_2 support) in the range 400-800 Ω/□ and mobilities in the 2000-3000 $cm^2V^{-1}s^{-1}$ range (with a p doping of few 10^{12} cm^{-2}). In order to characterize sample uniformity and polycrystallinity over larger areas, we validate the potential of a liquid crystal based polarizing optical microscopy technique as recently reported by Kim *et al.*[15] Figs. 3 h,i show polarizing optical microscopy (POM) images of a empty control and our reference MLG, respectively. The POM contrast is based on sample interactions with a 5CB nematic liquid crystal (See Supplementary Information). Across a 1 cm^2 MLG area POM indicates feature sizes ranging from ~40 $μm^2$ to a few hundred $μm^2$, which is consistent with the observed nuclei sizes of ~30-40 $μm^2$ in Fig. 1 and their subsequent merging. We note that all characterization above is done after graphene transfer, i.e. includes possible degradation incurred during transfer.

Whereas "optimized" CVD parameters can be highly system specific, we note that the variation of key parameters over a wide range offers fundamental insights into the growth process and allows the establishment of more generic growth guidelines. Fig. 4 shows results of our systematic exploration of the wider CVD parameter space and focuses on the effects of total pressure, growth time and hydrocarbon partial pressure, where for each experiment only one specified parameter was varied starting from the LPCVD benchmark recipe (see Fig. 3). The results are presented in terms of optical images of as-grown graphene films transferred to SiO_2 (300nm)/Si (Fig. 4 a-f) and corresponding Raman spectra (Fig. 4g). For a lower total pressure of 1 mbar only MLG and no FLG is observed, but for the given exposure the film has large holes (Fig. 4a). This is indicative of a lower graphene nucleation density and growth rate. We note that rather than focusing only on the carbon precursor and carbon addition, also competing etching processes, e.g. by H_2 or H_2O, have to be considered.[21,22] We clearly observe that as-grown graphene on Cu is etched while annealing in a H_2 atmosphere, which is the main reason why we do not use hydrogen during cool down, in contrast to other studies.[23]

1
2
3 We note that although this etching occurs in the presence of H_2 (at sufficiently high partial pressures), it may also arise from residual water or oxygen contamination.[8] 8 mbar of total pressure on the other hand leads to a significant increase in FLG nucleation and film inhomogeneity. An analogous behavior is seen for an increase in the CH_4 partial pressure (Fig. 4 e,f; Fig. 3a), where a 1:10 CH_4:H_2 results in incomplete MLG coverage and a 1:1 ratio shows significant multilayer coverage. In general, the lower the carbon precursor pressure the lower the likelihood of achieving complete MLG surface coverage.

Figs. 4 c,d combined with the reference sample in Fig. 3a show the effect of growth time: the longer the growth time the more complete the graphene coverage. Extended exposures, however, increase the fractional multilayer coverage. Importantly we find that new graphene layers can nucleate after the completion of a monolayer. We refer to this as secondary nucleation, as compared to the primary nucleation discussed above. In this context, we note that in Figs. 4 b, d, f the nucleation pattern of multilayered graphene appears to follow the rolling striations of the Cu foil. Fig. 4g shows that the interpretation of optical contrast in Figs. 4 a-f is in full agreement with measured Raman spectra corresponding to mono, bilayer (I_{2D}/I_G~1) and multilayer (I_{2D}/I_G<1) graphene. Further, the Raman measurements in Fig. 4g also confirm the interpretation of SEM contrast regarding multilayer graphene primary nucleation for APCVD conditions in Figs. 1e-h. The bilayer and FLG seen in areas of Fig. 4d-f show Raman spectra (Fig. 4g) corresponding to turbostratic graphene with 2D peaks that can be fitted with single Lorentzian peaks, whereas the APCVD conditions shows a Raman signature consistent with Bernal stacking.[20]

Figure 5 shows the results of LPCVD in undiluted CH_4 in order to assess the role of hydrogen dilution during growth in more detail. The post-growth Cu surface is dominated by triangular and other 3 lobed structures (Fig. 5 a-d), partly resembling a Sierpinski triangle like fractal pattern. An EBSD analysis (Fig. 2f) shows a predominant (111) texture for the processed Cu foil, whereby the triangles and lobed structures formed on Cu (111) facets and are not present on Cu (001). Attempts to transfer the structures to SiO_2/Si substrates resulted in small discontinuous patches of graphene and residual PMMA. Raman confirms the transferred patches as MLG (Fig. 5f). Importantly, Raman spectra (457 nm excitation) measured directly on the processed Cu foil show peaks corresponding to CuO (300 and 652 cm^{-1})[24,25]and CuO_2 (217, 415, 504, 808 cm^{-1})[24,25] for the triangular areas. The mechanisms of this self-organization are unclear, but we suggest it arises based on the balance of three competing

1
2
3
4
5
6
7
8
9
10
11
12
13
14
15
16
17
18
19
20
21
22
23
24
25
26
27
28
29
30
31
32
33
34
35
36
37
38
39
40
41
42
43
44
45
46
47
48
49
50
51
52
53
54
55
56
57
58
59
60

processes, namely graphene formation, its etching by residual oxygen and the formation of copper oxide from this residual oxygen. The parallel processes of reduction and oxidation could make the copper oxide species extremely mobile causing them to self-align in a triangular fashion due to the 3 fold symmetry of Cu (111).[26,27] Hence, our data shows that the presence of a hydrogen atmosphere suppresses the formation of Cu oxide from trace oxygen contamination during CVD. We note that the observation of triangular graphene on Cu(111) has been reported in recent literature,[26] without however considering the role of oxygen. This highlights why CH_4 as precursor requires H_2 dilution and our data above emphasized the delicate effects of the CH_4/H_2 balance.

Fig 2h shows that for LPCVD conditions at 1000°C the rate of Cu sublimation is significant and deleterious. Increasing the total pressure with an inert diluent can suppress the Cu sublimation, but, as discussed below, maintaining the CH_4/H_2 balance and achieving complete MLG coverage then becomes increasingly challenging.[28] The exponential variation of vapor pressure with temperature strongly motivates a temperature reduction to mitigate the Cu sublimation. Figs. 6 a-d show the effect of lowering the process temperature for CH_4 based graphene CVD on Cu. Comparing graphitic films grown at 1000, 900 and 800°C, the optical images of the transferred films all appear homogeneous (Fig. 6 a-c). The corresponding Raman spectra, however, show a significant deterioration in graphene quality, as highlighted by the significantly increased D peak intensity. The spectrum for 900°C shows ratios of I_{2D}/I_G of ~2.5 and I_D/I_G ~0.35. Also observed is the emergence of an additional defect peak, referred to as the D' peak,[29] near the G peak at higher wave numbers. A further reduction in temperature to 800°C leads to I_{2D}/I_G ~1.2 and $I_D/I_G > 2$ and a D' peak intensity increased to the level of the I_G peak. We also note that all these films are continuous, in contrast to recent literature that claims that no continuous films can be obtained below 1000°C at comparable experimental conditions.[23] Whereas the parameters discussed in Fig. 4 mainly influence the M/FLG ratio and coverage, growth temperature is clearly the most significant parameter influencing the crystalline quality of the as-grown material. Our data shows that with CH_4 as precursor the growth temperature cannot be lowered sufficiently to mitigate Cu sublimation and at the same time maintain a high graphene quality.

This raises the question of what fundamentally determines at how low a temperature can high quality graphene CVD be grown? We approach this question here by using benzene (C_6H_6) as an alternative carbon precursor. Fig. 6e shows the results of LPCVD, for which a simple

1
2
3
4
5
6
7
8
9
10
11
12
13
14
15
16
17
18
19
20
21
22
23
24
25
26
27
28
29
30
31
32
33
34
35
36
37
38
39
40
41
42
43
44
45
46
47
48
49
50
51
52
53
54
55
56
57
58
59
60

exposure to undiluted C_6H_6 was adopted. At 900°C, highly uniform MLG films of high quality (I_D/I_G ~0.06, Fig. 6e) are achieved with greatly reduced Cu sublimation compared to 1000°C. Analogous to Fig. 6d, the graphene quality decreases with decreasing growth temperature (Fig. 6 e). However the MLG quality for C_6H_6 based CVD is better at any given temperature (compare Figs. 6 d and e), and unlike for CH_4, graphitic material (albeit highly defective) nucleates at temperatures as low as 600°C for C_6H_6. Fig. 6f directly compares the measured I_D/I_G ratios for the two different carbon precursors. Raman maps for the C_6H_6 derived MLG 900°C show a uniform I_D/I_G ~0.06 and I_{2D}/I_G ~ 2.5 distribution over large area (dimensions 50 μm × 50 μm) as seen in Figs 7a-d. POM indicates a similar grain size distribution and polycrystallinity for the C_6H_6 derived MLG films (Figs. 7 i,j) as compared to the reference samples for CH_4/H_2 based CVD (Figs. 3 h,i). Further, 6 contact Hall geometry devices based on graphene grown from C_6H_6 at 900°C give sheet resistances (on SiO_2 support) in the range 400-800 Ω/□ and mobilities in the 2000-3000 $cm^2V^{-1}s^{-1}$ range (with a p doping of few 10^{12} cm^{-2}). These results highlight that C_6H_6 enables similar graphene quality at 100-150°C lower temperatures. i.e. that the apparent low temperature limit is precursor dependent.

The variation of CVD parameters over a wider parameter space for the benzene based process shows a similar general behavior compared to the CH_4 as precursor (Fig. 7 e-h). In particular, the lower the carbon precursor partial pressure the lower the likelihood of achieving complete MLG surface coverage, and the higher the exposure pressure the higher the likelihood of multilayer nucleation and film inhomogeneity. Again, the growth rate depends on the specific Cu surface. However, considering that between Figs. 7 e,f and g,h the C_6H_6 partial pressure increase was ~100 fold, the increase in fractional FLG coverage and inhomogeneity is surprisingly little. Significantly, we note that the partial pressure range in which C_6H_6 yields MLG (~10^{-4} –10^{-2} mbar) is much wider (relative to the partial pressure used) than for the CH_4 process (~0.2 - 1.5 mbar). Hence, for the conditions used, C_6H_6 as precursor does not require H_2 dilution and enables growth at lower temperatures with more robust processing conditions.

Discussion

The overall CVD process for graphene growth can be discussed in the context of basic heterogeneous catalysis and 2D crystal growth kinetics as a multistep reaction comprising:

1
2
3
4
5
6
7
8
9
10
11
12
13
14
15
16
17
18
19
20
21
22
23
24
25
26
27
28
29
30
31
32
33
34
35
36
37
38
39
40
41
42
43
44
45
46
47
48
49
50
51
52
53
54
55
56
57
58
59
60

(1) gaseous precursor transport to and dissociation on the catalyst surface, (2) transport of carbon (species) on the surface and into/out of bulk of the catalyst, (3) graphene nucleation and carbon incorporation into the growing graphene layer, (4) etching of the as-formed graphene. Step (1) thereby comprises transport of gas reactants through the boundary layer above the catalyst surface and the adsorption/desorption kinetics of the catalytic reaction. Simultaneous to its formation, (4) graphene etching can occur depending on the composition of the gas atmosphere and the presence of contaminants in the CVD set-up/process. The thermodynamic driving force for growth, i.e. step (3), is a carbon supersaturation at the catalyst surface.[16] In CVD this supersaturation is created via step (1), whereby the different CVD conditions can be expressed as different carbon chemical potentials. The chemical potential depends on temperature and partial pressures, which in turn depend on the choice of precursor and the reaction considered. A more reactive carbon source corresponds to carbon supplied at a higher chemical potential. We adopt this general framework here to qualitatively rationalize our findings, even though the experimental conditions might not be close to equilibrium, i.e. the carbon chemical potential is difficult to quantify.[30]

For carbon supplied at a very high chemical potential, graphene growth is very favorable and can become non-specific to details of the catalyst surface. Our data here (Figs. 1,4,7) is consistent with such a generic behavior insofar that the higher the supplied carbon chemical potential the higher the likelihood of film inhomogeneity and primary and secondary multilayer nucleation. Assuming growth occurs isothermally during CVD exposure and not during cool down (see below) and that additional layers grow in contact with the catalyst, i.e. underneath the existing graphene,[31,32] secondary nucleation indicates that carbon reaches the Cu surface even after complete MLG coverage. Isolated graphene flakes have been shown to be impermeable to gases,[33] hence we suggest that the observed carbon leakage is due to the inherent polycrystallinity of as-grown MLG whereby the domain boundaries and other defects offer pathways for the precursor to reach the catalyst. Hence clearly graphene CVD on Cu cannot be expected to inherently (independent of conditions applied) give a self-limiting homogeneous monolayer coverage. We emphasize that this has important ramifications for FLG CVD. Primary nucleation will not give a homogeneous FLG coverage due to the different growth rates of the layers. Secondary nucleation will require leakage through the covering layer(s), and the challenge is thereby to feed homogeneous growth

1
2
3
4
5
6
7
8
9
10
11
12
13
14
15
16
17
18
19
20
21
22
23
24
25
26
27
28
29
30
31
32
33
34
35
36
37
38
39
40
41
42
43
44
45
46
47
48
49
50
51
52
53
54
55
56
57
58
59
60

through inhomogeneous leakage. Further we expect the leakage to significantly decrease with the number of layers, so the number of layers possible is clearly limited by this method.

The more the supplied carbon chemical potential is lowered the more specific the graphene formation becomes to details of the catalyst surface, nature of nucleation sites, energy costs associated with graphene edges and for instance additional strain energies depending on the lattice mismatch.[30] Figs. 1 and 7 highlighted that graphene formation is indeed dependent on catalyst surface orientation and impurity levels. Improved growth on Cu(111) has been previously attributed to improved precursor adsorption and high diffusion of carbon species.[34] Compared to for instance Ni, Cu in its given state is a less active catalyst for step (1), hence higher temperatures are required to supply carbon at a given rate. Compared to CH_4, C_6H_6 represents a more reactive carbon source, which is captured in the temperature dependence of Fig. 6. Hence it is not surprising that we do not see any graphitic deposits at temperatures below 700°C for CH_4, whereas for C_6H_6 we observe carbon film deposition at temperatures as low as 300°C (see Fig. 6e) on Cu for the given conditions. Below 600°C, the crystallinity of the as-grown carbon is poor, and although the defect density will again depend on the detailed growth kinetics (e.g. carbon arrival rate vs incorporation rate), we cannot reproduce the Cu-catalyzed growth of graphene at temperature of 600°C or below, as recently reported for toluene[18](~ 600 °C, I_D/I_G~0.35) and ill-defined C_6H_6 exposures in hot-wall furnaces.[35] We note in this context that these previous efforts have focused on lowering the temperature, but clearly compromised on graphene quality.[18,35] Bearing in mind that graphene has to be transferred off the catalyst metal for most applications,[36] our motivation here is a temperature reduction while maintaining the quality.

Our data indicates that C_6H_6 as precursor does not only enable growth at lower temperatures but also more robust processing conditions. Some previous literature suggests that the 6-membered ring configuration of benzene would provide an inherent advantage, that could help to explain our findings.[35] However, even though the detailed nature of carbon species in steps (2) and (3) remains unknown, we see no evidence that the 6-membered ring configuration of C_6H_6 will be preserved at step (1) at the given conditions, as sometimes suggested in the literature.[35,37] Rather we suggest that the advantage of C_6H_6 lies in the rate balance that it allows during CVD. CH_4 requires H_2 dilution to reduce the Cu surface (Fig. 5) and the required CH_4/H_2 balance is critical (Fig. 4). We show that a lower CH_4/H_2 ratio leads to etching, hence the CH_4/H_2 balance reflects a balance between carbon deposition and

1 2 3 4 5 6 7 8 9 10 11 12 13 14 15 16 17 18 19 20 21 22 23 24 25 26 27 28 29 30 31 32 33 34 35 36 37 38 39 40 41 42 43 44 45 46 47 48 49 50 51 52 53 54 55 56 57 58 59 60

etching, i.e. between steps (3) and (4). We emphasize that this balance is highly process parameter dependent, which is why CH_4 based CVD is more delicate to control. At APCVD conditions, for instance, well known CVD kinetic models predict a mass transfer limited regime, whereby the boundary layer in step (1) is rate limiting. This has also been discussed in the context of graphene APCVD.[28] Based on our data, we suggest here that the delicate CH_4/H_2 balance shifts for pressure induced changes of the boundary layer and this is why achieving continuous MLG films based on APCVD is very challenging using CH_4 as precursor. C_6H_6 as precursor on the other hand is more reactive and requires no reactive diluent and related delicate balancing. We also suggest that diluting C_6H_6 with a neutral gas such as Ar should be much more straightforward than for CH_4 in terms of maintaining high quality graphene growth.

The above argumentation assumes that the observed graphene formation on Cu occurs predominantly during the precursor exposure at isothermal conditions, rather than due to precipitation upon cooling.[7,8] This assumption is supported by in-situ observations of isothermal graphene growth on Cu during elemental carbon deposition,[38] however the importance of the contribution of carbon precipitation on cooling should also be considered. Based on a simplistic consideration of carbon solubility in Cu at 1000°C of between 0.00070 at%[39] and 0.028 at% [40], the amount of carbon dissolved in the 25μm foil corresponds to between 0.4 and 15.5 layers of graphene with an atomic density of 3.8×10^{19} carbon atoms m^{-2}. It should be noted that the large uncertainties here reflect the significant disparities between the solubility values reported in the literature.[39,40] Realistically the diffusion lengths of carbon dissolution and precipitation may limit the active volume to some fraction of the foil thickness and should be considered when estimating whether the quantity of carbon that precipitates as graphene upon cooling is significant.[8] For such a calculation to be informative, a validation of the solubility and diffusivity of carbon in Cu is required which lies beyond the scope of the present work. We note that further in-situ experiments are needed to fully clarify the relative importance of growth by precipitation upon cooling.

Conclusions

We systematically explored the parameter space of graphene CVD on polycrystalline Cu foils in particular regarding the choice of carbon precursor and mitigation of Cu sublimation as

1
2
3
4
5
6
7
8
9
10
11
12
13
14
15
16
17
18
19
20
21
22
23
24
25
26
27
28
29
30
31
32
33
34
35
36
37
38
39
40
41
42
43
44
45
46
47
48
49
50
51
52
53
54
55
56
57
58
59
60

required towards industrial manufacture. CH_4, the currently most widely used carbon precursor, requires H_2 dilution and high temperatures (1000°C) to keep the Cu surface reduced and yield high quality graphene. The H_2 atmosphere etches as-grown graphene, hence maintaining a balanced CH_4/H_2 ratio is critical. Such balance is more easily achieved at low pressure conditions, at which however Cu sublimation is at deleterious levels. In contrast, C_6H_6 as precursor requires no reactive dilution, i.e. no delicate balance to be maintained, and consistently gives similar graphene quality at 100-150°C lower temperatures compared to CH_4 based CVD. The lower process temperature and more robust processing conditions allow the problem of Cu sublimation to be effectively addressed. Our growth study shows that Cu is not inherently limiting graphene formation to a monolayer. Rather the higher the supplied carbon chemical potential the higher the likelihood of film inhomogeneity and primary and secondary multilayer nucleation. Secondary nucleation indicates that carbon reaches the Cu surface even after complete MLG coverage, whereby we suggest that the domain boundaries of the inherently polycrystalline layers offer pathways for the precursor to reach the catalyst. Our data further emphasizes that the Cu catalyst template is not static and that the involved kinetics of grain growth are highly process dependent, making this an important process step for controlled graphene CVD.

Although the data presented concerns only two carbon precursors, we expect the insights achieved to be of general relevance for the optimization of graphene CVD and more rational process design. While C_6H_6 may not be the precursor of choice for industrial upscaling due to its harmful effects on health, we think that it serves as a good model precursor system to effectively study the effect of precursor reactivity for graphene CVD. We have preliminary data for xylene as carbon precursor, which is an example of a cheap and safe precursor that shows similar advantages as highlighted here for benzene, in particular giving MLG at 900°C when diluted in Ar at APCVD conditions without Cu sublimation.

Acknowledgements

S.H. acknowledges funding from ERC grant InsituNANO (n°279342) and from EPSRC (Grant Nr. EP/H047565/1). P.R.K. acknowledges funding from the Cambridge Commonwealth Trust and C.D. acknowledges funding from Royal Society. The authors wish to acknowledge Dr. Matt Cole for help with equipment modification, Amalya Kostanyan for help with the POM characterization, and Dr. Bernhard C. Bayer for discussions.

Supporting Information

More experimental details on the EBSD analysis and on the liquid crystal based polarizing optical microscopy (POM) technique are available as supporting information. This information is available free of charge via the Internet at http://pubs.acs.org.

ACS Paragon Plus Environment

References

(1) Dresselhaus, M. S.; Dresselhaus, G.; Avouris, P. *Carbon nanotubes: synthesis, structure, properties, and applications*; Springer, **2001**.

(2) Hiruma, K.; Yazawa, M.; Katsuyama, T.; Ogawa, K.; Haraguchi, K.; Koguchi, M.; Kakibayashi, H. *J. Appl. Phys.* **1995**, *77*, 447-62.

(3) Hofmann, S.; Sharma, R.; Ducati, C.; Du, G.; Mattevi, C.; Cepek, C.; Cantoro, M.; Pisana, S.; Parvez, A.; Cervantes-Sodi, F.; et al. *Nano Lett.* **2007**, *7*, 602–8.

(4) Li, X.; Cai, W.; An, J.; Kim, S.; Nah, J.; Yang, D.; Piner, R.; Velamakanni, A.; Jung, I.; Tutuc, E.; et al. *Science* **2009**, *324*, 1312–4.

(5) Bae, S.; Kim, H.; Lee, Y.; Xu, X.; Park, J.S.; Zheng, Y.; Balakrishnan, J.; Lei, T.; Kim, H. R.; Song, Y. I.; et al. *Nat. Nanotechnol.* **2010**, *5*, 574–8.

(6) Li, X.; Cai, W.; Colombo, L.; Ruoff, R. S. *Nano Lett.* **2009**, *9*, 4268–72.

(7) Weatherup, R. S.; Bayer, B. C.; Blume, R.; Ducati, C.; Baehtz, C.; Schlögl, R.; Hofmann, S. *Nano Lett.* **2011**, *11*, 4154–60.

(8) Weatherup, R. S.; Bayer, B. C.; Blume, R.; Baehtz, C.; Kidambi, P. R.; Fouquet, M.; Wirth, C. T.; Schlögl, R.; Hofmann, S. *Chemphyschem.* **2012**,10,2544-49.

(9) Regmi, M.; Chisholm, M. F.; Eres, G. *Carbon.* **2012**, *50*, 134–141.

(10) Huang, P. Y.; Ruiz-Vargas, C. S.; Zande, A. M. van der; Whitney, W. S.; Levendorf, M. P.; Kevek, J. W.; Garg, S.; Alden, J. S.; Hustedt, C. J.; Zhu, Y.; et al. *Nature* **2011**, *469*, 389–92.

(11) Kim, K.; Lee, Z.; Regan, W.; Kisielowski, C.; Crommie, M. F.; Zettl, A. *ACS Nano.* **2011**, *5*, 2142–6.

(12) Petrone, N.; Dean, C. R.; Meric, I.; Zande, A. M. van der; Huang, P. Y.; Wang, L.; Muller, D.; Shepard, K. L.; Hone, J. *Nano Lett.* **2012**, *12*, 2751–6.

(13) Li, X.; Magnuson, C. W.; Venugopal, A.; Tromp, R. M.; Hannon, J. B.; Vogel, E. M.; Colombo, L.; Ruoff, R. S. *J. Am. Chem. Soc.* **2011**, *133*, 2816–9.

(14) Ismach, A.; Druzgalski, C.; Penwell, S.; Schwartzberg, A.; Zheng, M.; Javey, A.; Bokor, J.; Zhang, Y. *Nano Lett.* **2010**, *10*, 1542–8.

(15) Kim, D. W.; Kim, Y. H.; Jeong, H. S.; Jung, H.-T. *Nat. Nanotechnol.* *7*, 29–34.

(16) Batzill, M. *Surf. Sci. Rep.* **2012**, *67*, 83–115.

(17) Li, X.; Magnuson, C. W.; Venugopal, A.; An, J.; Suk, J. W.; Han, B.; Borysiak, M.; Cai, W.; Velamakanni, A.; Zhu, Y.; et al. *Nano Lett.* **2010**, *10*, 4328–34.

(18) Zhang, B.; Lee, W. H.; Piner, R.; Kholmanov, I.; Wu, Y.; Li, H.; Ji, H.; Ruoff, R. S. *ACS Nano.* **2012**,6,2471-76.

(19) Humphreys, F. J.; Hatherly, M. *Recrystallization and Related Annealing Phenomena* Elsevier, **2004**.

(20) Ferrari, A. C.; Meyer, J. C.; Scardaci, V.; Casiraghi, C.; Lazzeri, M.; Mauri, F.; Piscanec, S.; Jiang, D.; Novoselov, K. S.; Roth, S.; et al. *Phys. Rev. Lett. 97*, 187401.

(21) Zhang, Y.; Li, Z.; Kim, P.; Zhang, L.; Zhou, C. *ACS Nano.* **2012**, *6*, 126–32.

(22) Vlassiouk, I.; Regmi, M.; Fulvio, P.; Dai, S.; Datskos, P.; Eres, G.; Smirnov, S. *ACS Nano.* **2011**, *5*, 6069–76.

(23) Kim, H.; Mattevi, C.; Calvo, M. R.; Oberg, J. C.; Artiglia, L.; Agnoli, S.; Hirjibehedin, C. F.; Chhowalla, M.; Saiz, E. *ACS Nano.* **2012**, 6, 3614–23.

(24) Rackauskas, S.; Nasibulin, A. G.; Jiang, H.; Tian, Y.; Kleshch, V. I.; Sainio, J.; Obraztsova, E. D.; Bokova, S. N.; Obraztsov, A. N.; Kauppinen, E. I. *Nanotechnology* **2009**, *20*, 165603.

(25) Hamilton, J. C. *J. Electrochem. Soc.* **1986**, *133*, 739.

(26) Liu, J.; Wu, J.; Edwards, C. M.; Berrie, C. L.; Moore, D.; Chen, Z.; Maroni, V. A.; Paranthaman, M. P.; Goyal, A. *Adv. Funct. Mater.* **2011**, *21*, 3868–3874.

(27) Wiame, F.; Maurice, V.; Marcus, P. *Surf. Sci. 601*, 1193–1204.

(28) Bhaviripudi, S.; Jia, X.; Dresselhaus, M. S.; Kong, J. *Nano Lett. 10*, 4128–4133.

(29) Cançado, L. G.; Jorio, A; Ferreira, E. H. M.; Stavale, F.; Achete, C. A; Capaz, R. B.; Moutinho, M. V. O.; Lombardo, A; Kulmala, T. S.; Ferrari, A. C. *Nano Lett.* **2011**, *11*, 3190–6.

(30) Saadi, S.; Abild-Pedersen, F.; Helveg, S.; Sehested, J.; Hinnemann, B.; Appel, C. C.; Nørskov, J. K. *J. Phys. Chem. C* **2010**, *114*, 11221–27.

(31) Nie, S.; Wu, W.; Xing, S.; Yu, Q.; Mccarty, K. F.; arXiv:1202.1031v2.

(32) Nie, S.; Walter, A. L.; Bartelt, N. C.; Starodub, E.; Bostwick, A.; Rotenberg, E.; McCarty, K. F. *ACS Nano.* **2011**, *5*, 2298–306.

(33) Bunch, J. S.; Verbridge, S. S.; Alden, J. S.; Zande, A. M. van der; Parpia, J. M.; Craighead, H. G.; McEuen, P. L. *Nano Lett.* **2008**, *8*, 2458–62.

(34) Wood, J. D.; Schmucker, S. W.; Lyons, A. S.; Pop, E.; Lyding, J. W. *Nano. Lett.* **2011**, *9*, 4547-54.

(35) Li, Z.; Wu, P.; Wang, C.; Fan, X.; Zhang, W.; Zhai, X.; Zeng, C.; Li, Z.; Yang, J.; Hou, J. *ACS Nano.* **2011**, *5*, 3385–90.

(36) Kidambi, P. R.; Bayer, B. C.; Weatherup, R. S.; Ochs, R.; Ducati, C.; Szabó, D. V.; Hofmann, S. *Phys. Status Solidi (RRL).* **2011**, *9*, 341–343.

(37) Yang, Y.; Hu, Z.; Tian, Y. J.; L, Y. N.; Wang, X. Z.; Chen, Y. *Nanotechnology.* **2003**, *14*, 733–737.

(38) Wofford, J. M.; Nie, S.; McCarty, K. F.; Bartelt, N. C.; Dubon, O. D. *Nano Lett.* **2010**, *10*, 4890–96.

(39) López, G. A.; Mittemeijer, E. J. *Scr. Mater.* **2004**, *51*, 1–5.

(40) Mclellan, R. B. *Scripta Metallurgica* **1969**, *3*, 389–391.

1
2
3
4
5
6
7
8
9
10
11
12
13
14
15
16
17
18
19
20
21
22
23
24
25
26
27
28
29
30
31
32
33
34
35
36
37
38
39
40
41
42
43
44
45
46
47
48
49
50
51
52
53
54
55
56
57
58
59
60

Figure Captions

Figure 1. SEM images at different magnification showing graphene nuclei on Cu before merging to form a continuous film a), b) Monolayer nuclei LPCVD 4 mbar, 1000°C, (1:10) CH_4 : H_2 for 25 min before merging to form a continuous film on 99.999% pure 25 μm foil c),d) multilayer nuclei LPCVD 4 mbar, 1000°C (1:1) CH_4 : H_2 for 5 min on 99.999% pure 25 μm foil e),f) multilayer nuclei LPCVD 4 mbar, 1000°C (1:1) CH_4 : H_2 for 5 min on 99.999% pure 100 μm foil with the underlying Cu grain orientation measured by EBSD g),h) multilayer nuclei APCVD 1000°C (1:25) CH_4 : H_2 for 5 min on 99.999% pure 25 μm foil i),j) multilayer nuclei APCVD 1000°C (1:25) CH_4 : H_2 for 5 min on 99.995% pure 12 μm Cu foil.

Figure 2. SEM images with EBSD in spot mode showing the evolution of the Cu catalyst for different growth conditions. a) as received 99.999% pure 25 μm foil, b) after APCVD anneal for 10 min at 1000°C, c) after LPCVD anneal for 10 min at 1000°C min at 4 mbar, d) after APCVD growth at 1000°C (1:25) CH_4 : H_2 for 5 min e) after LPCVD growth at 1000°C, 4 mbar (1:5) CH_4 : H_2 for 30 min, f) after LPCVD growth 1000°C, 4 mbar (1:0) CH_4 : H_2 for 30 min. Optical images of the furnace tube g) after processing at APCVD and h) 4 mbar and 1000°C respectively.

Figure 3. Characterization of large area MLG film grown in LPCVD 4 mbar, 1000°C, (1:5) CH_4 : H_2 for 30 min on 99.999% pure 25 μm foil a) Optical image b) Raman spectrum confirms the presence of MLG. Raman map of large area MLG c) I_{2D}/I_G d) I_D/I_G and e) and f) show the corresponding distribution statistics. g) 6 contacts Hall geometry devices. h) Control Polarizing microscopy (POM) image in a region of the sample containing no graphene. i) POM image, for liquid crystal (LC) over graphene sample.

Figure 4. Optical image of graphene film grown on 99.999% pure 25 μm foil by LPCVD and transferred to SiO_2(300 nm)/Si a) 1 mbar and b) 8 mbar at 1000°C, (1:5) CH_4 : H_2 for 30 min. c) 10 min and d) 60 min at 4 mbar, 1000°C, (1:5) CH_4 : H_2, e) (1:10) and f) (1:1) at CH_4 : H_2, 4 mbar, 1000°C, for 30 min. g) Raman spectra for mono, bi and multilayer seen in Fig 4a-f marked with the corresponding color of the circle and APCVD FLG graphene seen in Fig 1g-j.

1
2
3
4
5
6
7
8
9
10
11
12
13
14
15
16
17
18
19
20
21
22
23
24
25
26
27
28
29
30
31
32
33
34
35
36
37
38
39
40
41
42
43
44
45
46
47
48
49
50
51
52
53
54
55
56
57
58
59
60

Figure 5. LPCVD growth in the absence of H_2 at 4 mbar, CH_4:H_2 (1:0), 1000°C for 30 min a),b) optical images of Cu foil post growth c),d) SEM images of Cu foil post growth e) optical images post transfer to SiO_2(300nm)/Si wafer f) Raman spectra measured on the triangular structure on the Cu foil (red, 457nm laser) and post transfer to SiO2(300nm)/Si wafer (blue).

Figure 6. Optical images of graphitic film grown on Cu at 4mbar, 1:5 CH_4 : H_2,30 min at a) 1000, b) 900 and c) 800°C and d) shows the corresponding Raman spectra marked with the respective color. e) Shows Raman spectra measured on graphitic films grown with C_6H_6 at different temperatures post transfer to a SiO_2(300nm)/Si wafer. f) I_D/I_G ratios for graphitic films grown from CH_4 (squares) and C_6H_6 (circles). Optical images of a graphitic film grown on Cu at with C_6H_6 at g) 900, h) 800 and i) 300°C post transfer to a SiO_2(300nm)/Si wafer.

Figure 7. Raman map for of large area MLG films grown from C_6H_6 at LPCVD conditions at 900°C on 99.999% pure 25 μm foil a) I_{2D}/I_G maps b) I_D/I_G maps. c) and d) show the corresponding distribution statistics. SEM images at different magnifications showing graphene nuclei on Cu from C_6H_6 at LPCVD conditions at 900°C on 99.999% pure 25 μm foil for e),f) at low exposure conditions with C_6H_6 partial pressure ~ 10^{-4} mbar for 5 min and g),h) at high exposure conditions with C_6H_6 partial pressure ~10^{-2} mbar for 5 min. i),j) h) POM images for liquid crystal (LC) over C_6H_6 derived graphene sample at different rotations highlighting the polycrystallinity of the MLG.

ACS Paragon Plus Environment

1
2
3 **Figures**
4
5
6
7
8
9
10
11
12
13
14
15
16
17
18
19
20
21
22
23
24
25
26
27
28
29
30
31
32
33
34
35
36
37
38
39

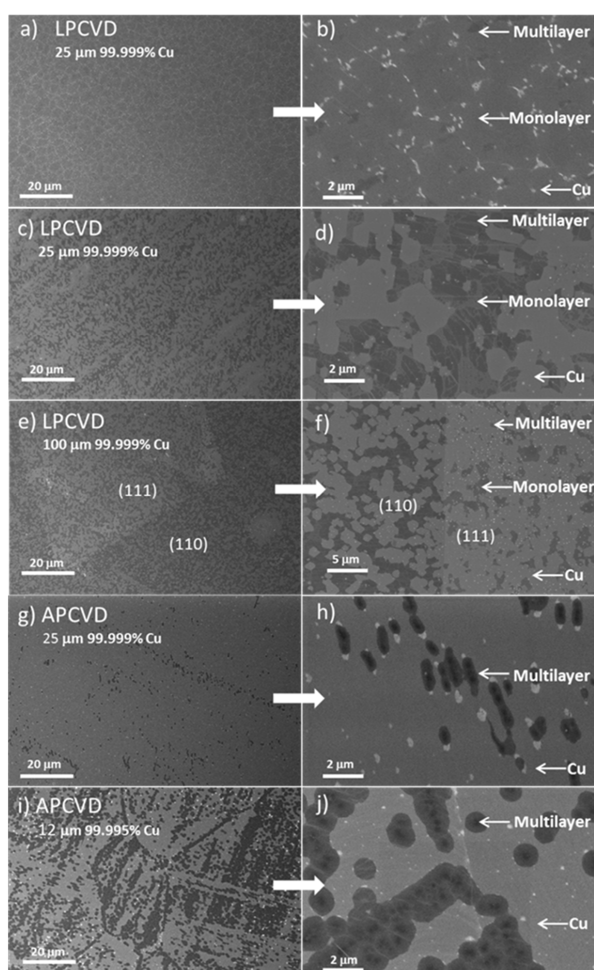

40 Figure 1 Kidambi et al.
41
42
43
44
45
46
47
48
49
50
51
52
53
54
55
56
57
58
59
60

1
2
3
4
5
6
7
8
9
10
11
12
13
14
15
16
17
18
19
20
21
22
23
24
25
26
27
28
29
30
31
32
33
34
35
36
37
38
39
40
41
42
43
44
45
46
47
48
49
50
51
52
53
54
55
56
57
58
59
60

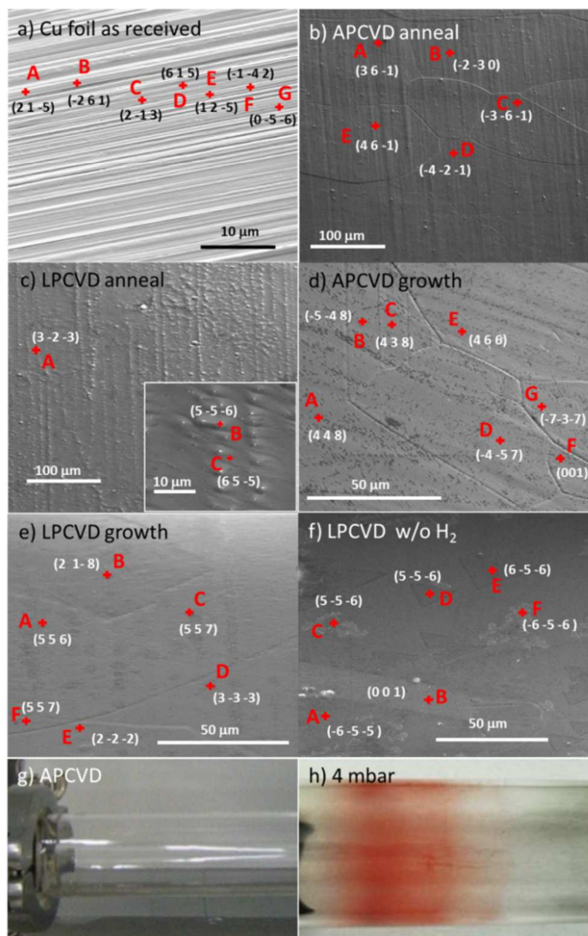

Figure 2 Kidambi et al.

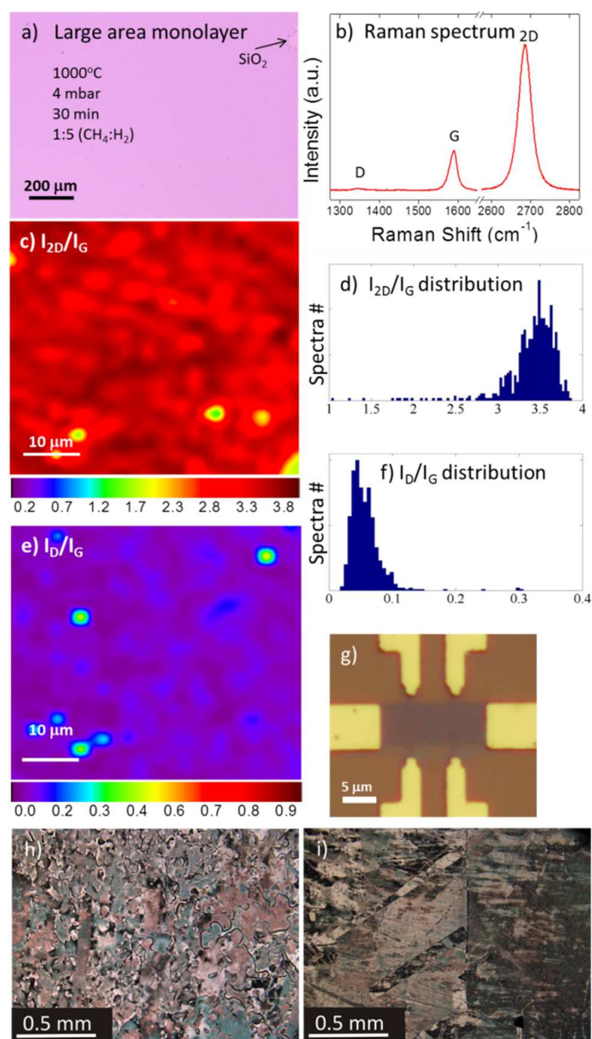

Figure 3 Kidambi et al.

1
2
3
4
5
6
7
8
9
10
11
12
13
14
15
16
17
18
19
20
21
22
23
24
25
26
27
28
29
30
31
32
33
34
35
36
37
38
39
40
41
42
43
44
45
46
47
48
49
50
51
52
53
54
55
56
57
58
59
60

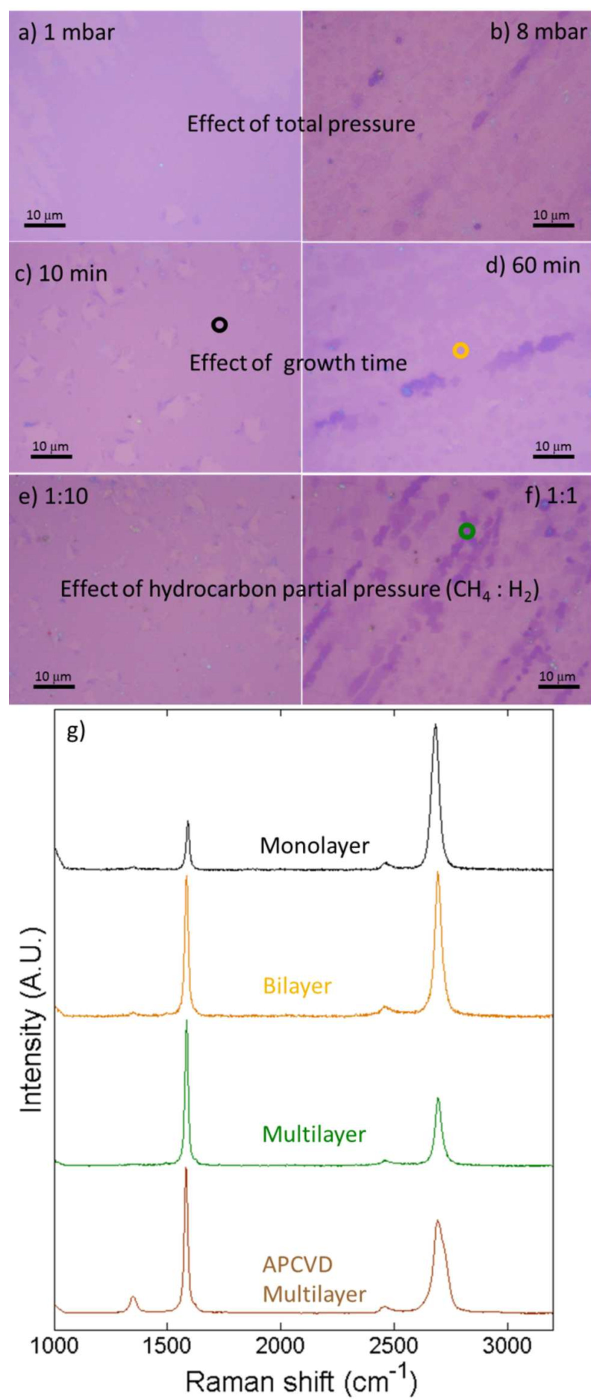

Figure 4 Kidambi et al.

1
2
3
4
5
6
7
8
9
10
11
12
13
14
15
16
17
18
19
20
21
22
23
24
25
26
27
28
29
30
31
32
33
34
35
36
37
38
39
40
41
42
43
44
45
46
47
48
49
50
51
52
53
54
55
56
57
58
59
60

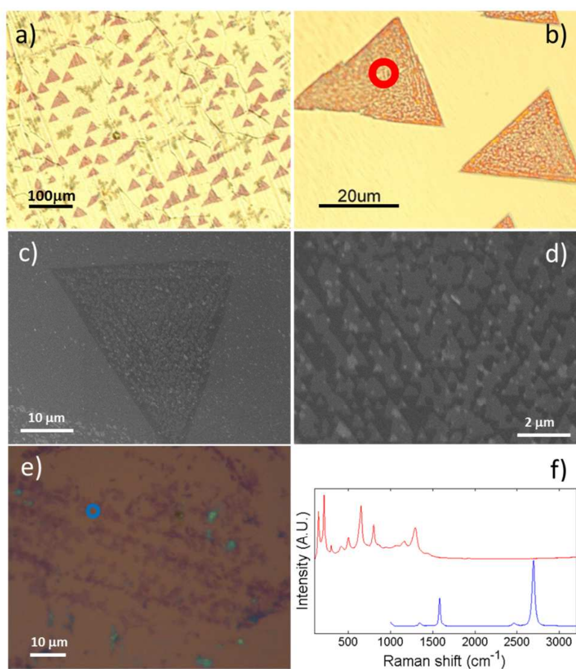

Figure 5 Kidambi et al.

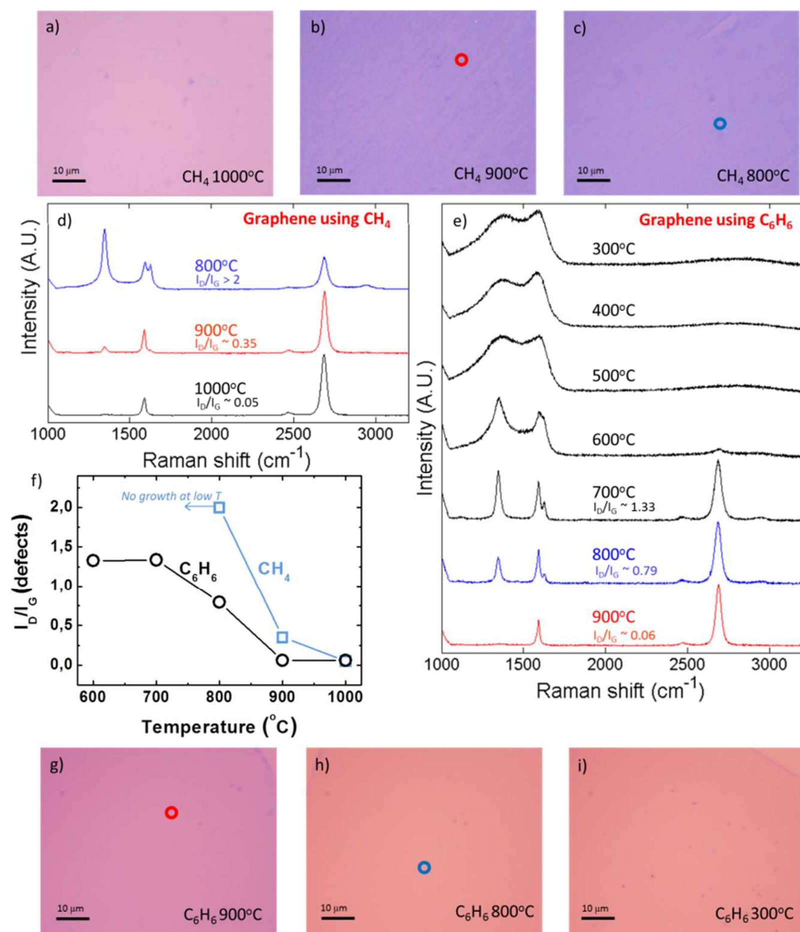

Figure 6 Kidambi et al.

1
2
3
4
5
6
7
8
9
10
11
12
13
14
15
16
17
18
19
20
21
22
23
24
25
26
27
28
29
30
31
32
33
34
35
36
37
38
39
40

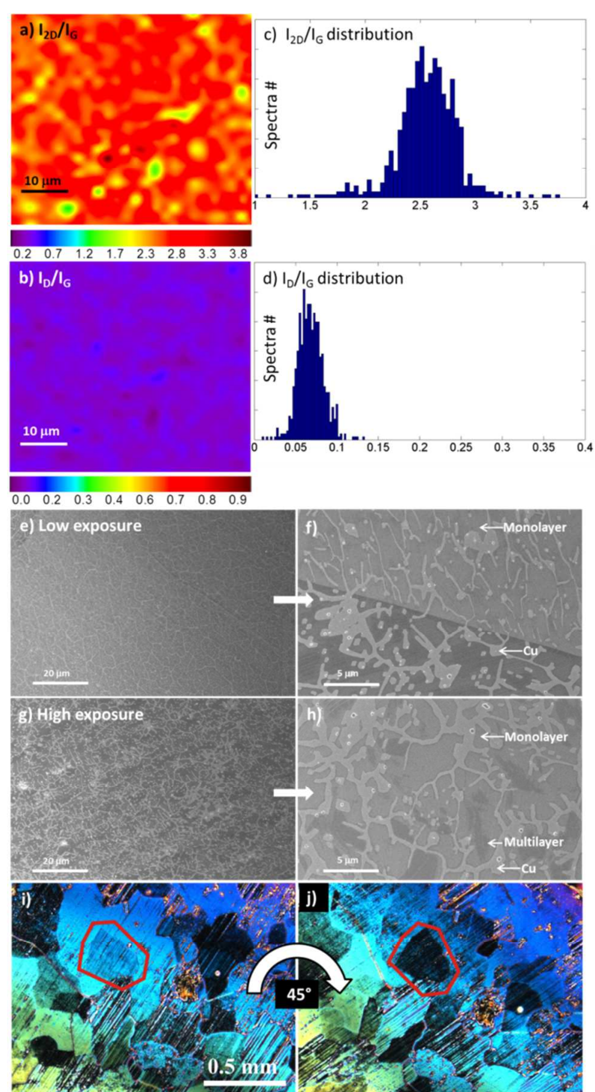

41
42
43
44
45
46
47
48
49
50
51
52
53
54
55
56
57
58
59
60

Figure 7 Kidambi et al.

1
2
3
4
5
6
7
8
9
10
11
12
13
14
15
16
17
18
19
20
21
22
23
24
25
26
27
28
29
30
31
32
33
34
35
36
37
38
39
40
41
42
43
44
45
46
47
48
49
50
51
52
53
54
55
56
57
58
59
60

Table of Contents Graphic

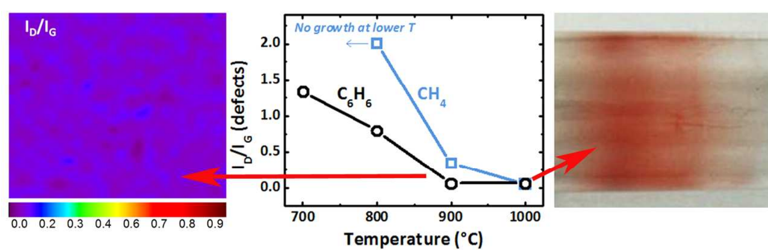

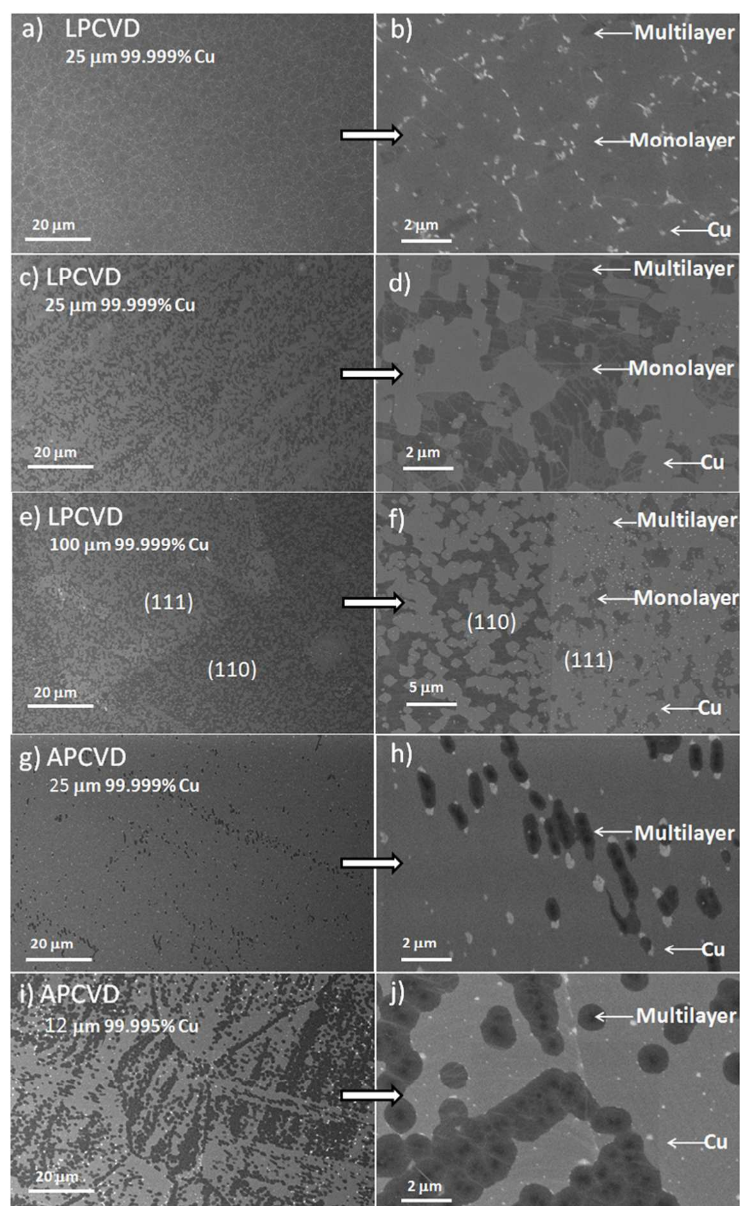

70x114mm (300 x 300 DPI)

1
2
3
4
5
6
7
8
9
10
11
12
13
14
15
16
17
18
19
20
21
22
23
24
25
26
27
28
29
30
31
32
33
34
35
36
37
38
39
40
41
42
43
44
45
46
47
48
49
50
51
52
53
54
55
56
57
58
59
60

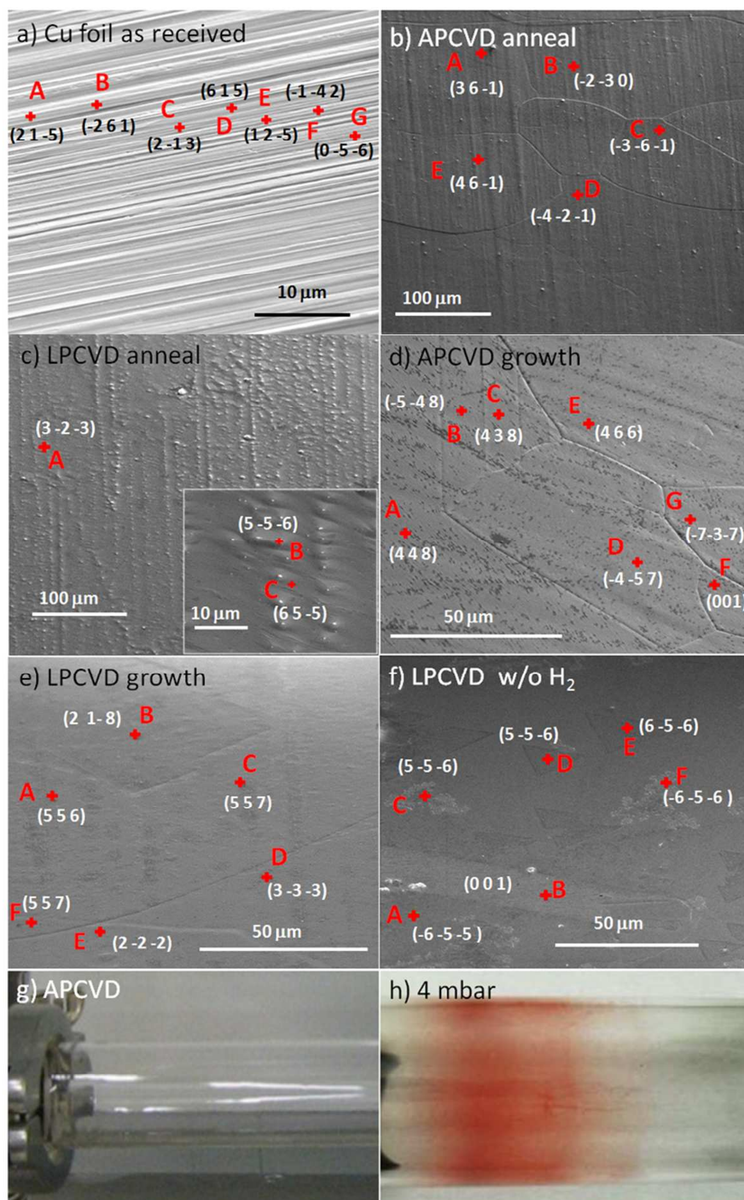

70x110mm (300 x 300 DPI)

1
2
3
4
5
6
7
8
9
10
11
12
13
14
15
16
17
18
19
20
21
22
23
24
25
26
27
28
29
30
31
32
33
34
35
36
37
38
39
40
41
42
43
44
45
46
47
48
49
50
51
52
53
54
55
56
57
58
59
60

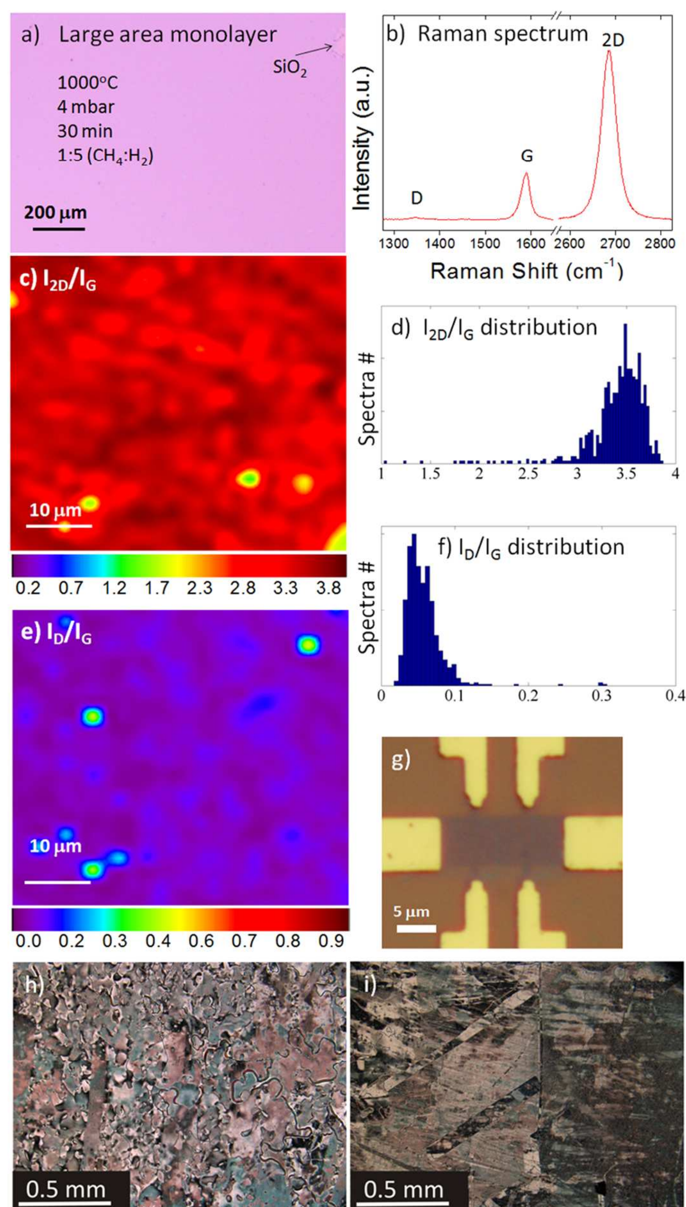

70x123mm (300 x 300 DPI)

1
2
3
4
5
6
7
8
9
10
11
12
13
14
15
16
17
18
19
20
21
22
23
24
25
26
27
28
29
30
31
32
33
34
35
36
37
38
39
40
41
42
43
44
45
46
47
48
49
50
51
52
53
54
55
56
57
58
59
60

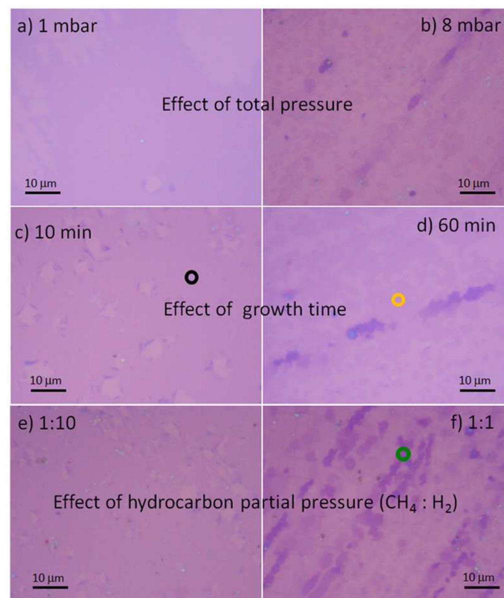

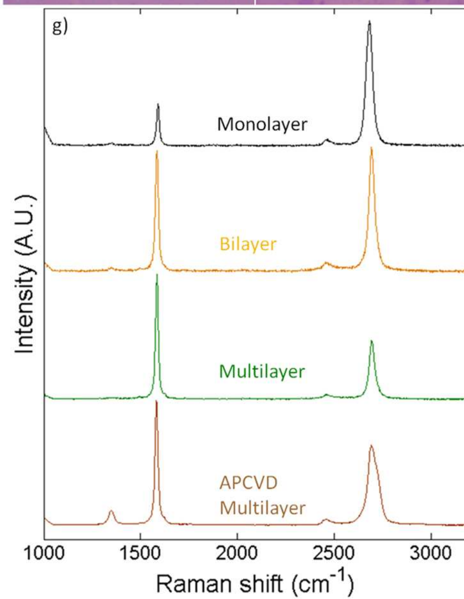

60x141mm (300 x 300 DPI)

1
2
3
4
5
6
7
8
9
10
11
12
13
14
15
16
17
18
19
20
21
22
23
24
25
26
27
28
29
30
31
32
33
34
35
36
37
38
39
40
41
42
43
44
45
46
47
48
49
50
51
52
53
54
55
56
57
58
59
60

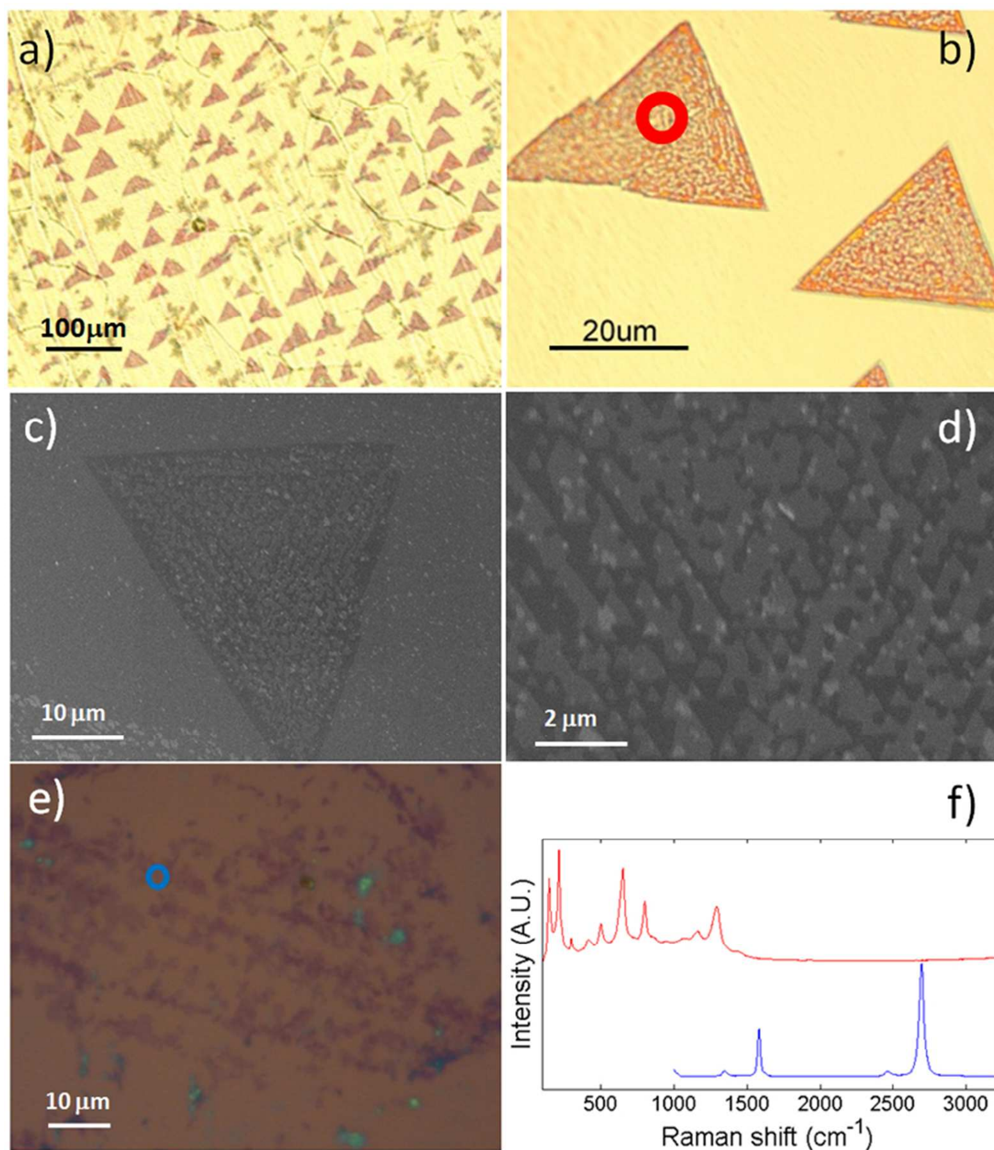

70x80mm (300 x 300 DPI)

1
2
3
4
5
6
7
8
9
10
11
12
13
14
15
16
17
18
19
20
21
22
23
24
25
26
27
28
29
30
31
32
33
34
35
36
37
38
39
40
41
42
43
44
45
46
47
48
49
50
51
52
53
54
55
56
57
58
59
60

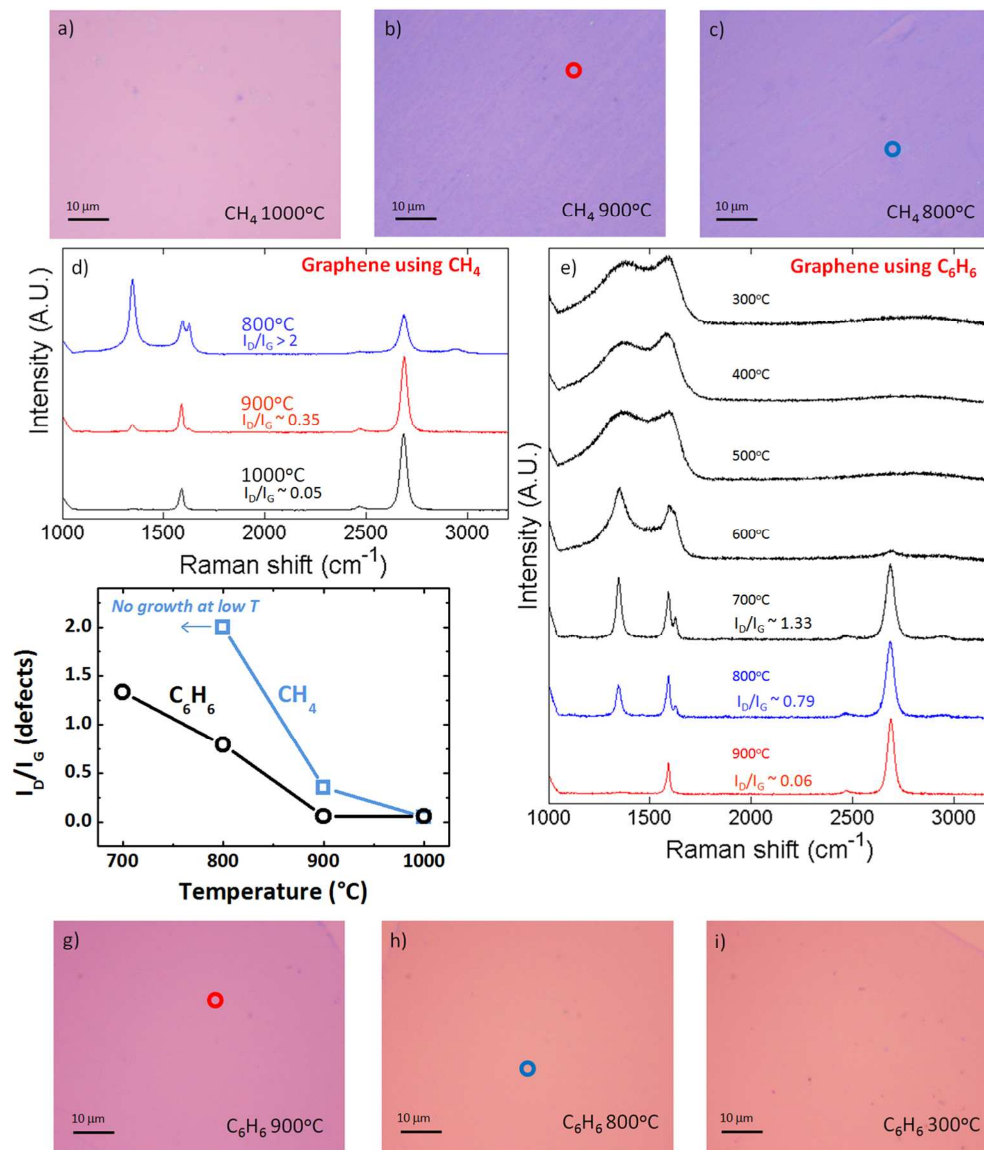

119x137mm (300 x 300 DPI)

1
2
3
4
5
6
7
8
9
10
11
12
13
14
15
16
17
18
19
20
21
22
23
24
25
26
27
28
29
30
31
32
33
34
35
36
37
38
39
40
41
42
43
44
45
46
47
48
49
50
51
52
53
54
55
56
57
58
59
60

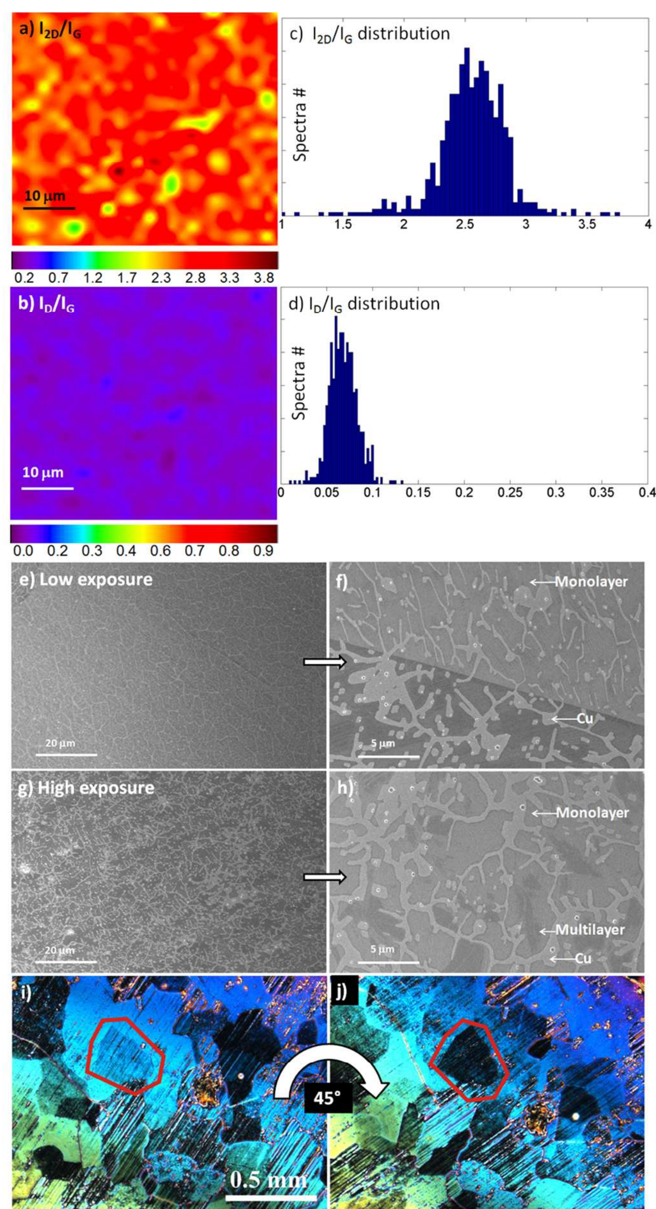

80x146mm (300 x 300 DPI)

1
2
3
4
5
6
7
8
9
10
11
12
13
14
15
16
17
18
19
20
21
22
23
24
25
26
27
28
29
30
31
32
33
34
35
36
37
38
39
40
41
42
43
44
45
46
47
48
49
50
51
52
53
54
55
56
57
58
59
60

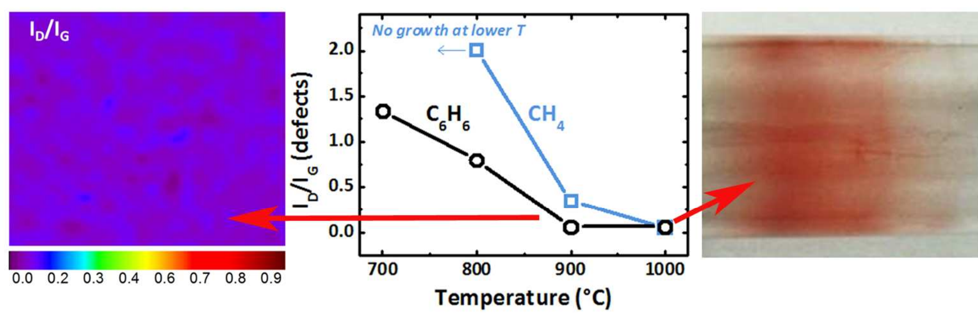

570x180mm (72 x 72 DPI)